Microwave Imaging for the Diagnosis of Cervical Diseases: A Feasibility Analysis

Chiara Dachena, Alessandro Fedeli, *Member, IEEE*, Alessandro Fanti, *Member, IEEE,* Matteo B. Lodi, *Student Member, IEEE*, Matteo Pastorino, *Fellow, IEEE*, and Andrea Randazzo, *Senior Member, IEEE*

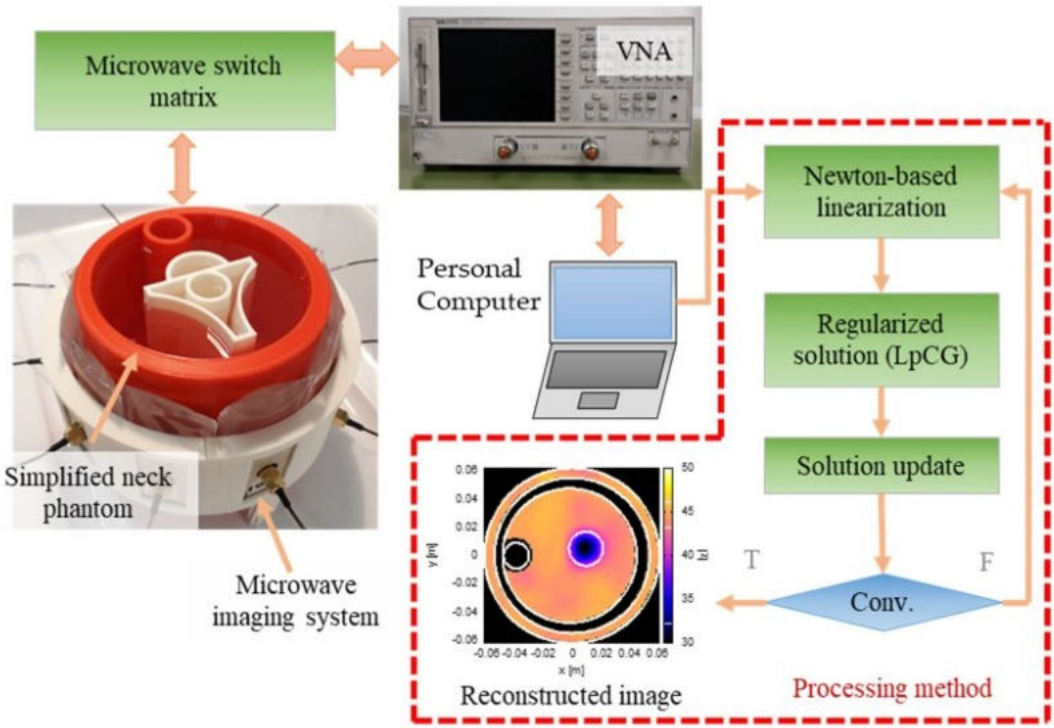

Microwave imaging system, neck phantom and processing method for the assessment of cervical diseases.

Take-Home Messages

- The possibility of performing noninvasive diagnosis of cervical diseases by using microwave imaging systems is explored in this paper.
- A feasibility analysis has been conducted by considering both numerical and simplified experimental phantoms, showing good capabilities in reconstructing 2D images of the neck.
- The envisioned technique could be useful for monitoring different diseases affecting the neck (e.g., cervical myelopathy) in a safe and less expensive way, thus allowing a frequent use.
- The obtained results, although still preliminary, show that it is in principle possible to identify the cervical spinal canal inside neck models, opening new grounds for the application of microwave imaging to biomedical diagnostics.
- An initial imaging prototype has been presented, comprising a set of transmitting/receiving antennas held in contact with neck by means of a 3D printed collar as well as an efficient inverse scattering technique based on a nonlinear Newton-type algorithm for reconstructing neck images. Moreover, a 3D-printed liquid-filled simplified phantom of the neck has been created to aid the preliminary assessment of the proposed technique.

Microwave Imaging for the Diagnosis of Cervical Diseases: A Feasibility Analysis

Chiara Dachena, Alessandro Fedeli, *Member, IEEE*, Alessandro Fanti, *Member, IEEE,* Matteo B. Lodi, *Student Member, IEEE*, Matteo Pastorino, *Fellow, IEEE*, and Andrea Randazzo, *Senior Member, IEEE*

Abstract: An inverse scattering method working at microwave frequencies for cervical diagnostics is proposed in this work. The aim is the diagnosis of cervical myelopathy, which is a disease that affects the first part of the spinal cord (between the C3 and C7 vertebra). A preliminary feasibility analysis oriented toward the development of an imaging system is reported. The system prototype includes a set of antennas that illuminate the neck and retrieve samples of the scattered electric field. The related inverse scattering problem is solved by using a nonlinear Newton-type reconstruction procedure, which provides two-dimensional images of the dielectric parameters of a neck cross section. A simplified cylindrical phantom mimicking the human neck has been designed for assessing the feasibility of the envisioned microwave measurement system and processing technique. Numerical results are reported to evaluate the capabilities of the proposed approach. Moreover, initial experimental results have been obtained by using cylindrical containers and a 3D printed version of the developed neck phantom.

Keywords **— Microwave imaging, inverse problems, spinal cord, tomography.**

I. Introduction

THE use of microwave radiation as a tool to support diagnostic processes has emerged some decades ago, together with the development of the first system prototypes [1]. The range of potential applications is nowadays wide and covers security, environmental and civil engineering, non-destructive testing, and biomedical imaging [2]–[7], as also confirmed by the many technical and clinical reviews in this latter area [8]–[13]. In the medical field, one of the first applications of microwave imaging (MWI) was the detection of breast tumors [14]–[23]. Subsequently, brain stroke detection has been considered [24]–[26], too. In this framework, several techniques and system prototypes have been developed [27]–[35] and some clinical tests have already been started [36]–[40]. However, breast cancer and brain stroke detection are not the unique promising medical applications: other possible usages include imaging of torso, arms, and other body parts [41]–[44].

An interesting and rather unexplored field is represented by MWI of the human neck. Several pathologic conditions can affect this part of the body, and a non-invasive and safe imaging method can be useful for monitoring patients. Indeed, as shown in [45], more than 50% of the middle-age population shows radiographic signals of cervical disorder. One of the common causes is cervical myelopathy [46], which is a disease that damages the first part of the spinal cord, between the C3 and C7 cervical vertebrae located near the head [47]. Because of its important function, the spinal cord is protected inside the spinal canal, which is formed by the collection of all the vertebral foramina [48]. A reduction of the spinal canal sagittal diameter, which may be caused by different factors [49], is the first effect of cervical myelopathy. Indeed, as shown in [47], [50], the physiological diameter of the spinal canal is around 18 mm and its reduction of ~25% is associated to this pathology. Some patients are asymptomatic and for this reason continuous monitoring is important and necessary to control the pathology progression. The gold-standard diagnostic methods are computerized tomography (CT), nuclear magnetic resonance (NMR) and X-rays [47], [51]. However, X-rays and CT could be cancerogenic due to their ionizing radiations [52], whilst NMR is expensive and slow [53], [54]. Consequently, frequent monitoring with these techniques is not cost effective, motivating the study of complementary diagnostic techniques. Microwave techniques are deemed quite interesting, since they use safe non-ionizing radiations and require low-cost components, being the frequency range the same of other wide-spread apparatuses [55]. Although different setups and processing techniques have been proposed for specific body parts (e.g., breast and head), other conformations usually require ad-hoc designed systems and data inversion procedures. More importantly, it is necessary to analyze their capabilities in retrieving the needed information about the parts of interest.

Some preliminary exploratory studies concerning microwave neck imaging have been presented in [56], where a simplified structure resembling the neck is discussed, and in [57], where qualitative techniques are used for detecting thyroid tumors. In [58], the impact of the spinal canal size on transmission measurements has been

C. Dachena, A. Fedeli, M. Pastorino, and A. Randazzo are with the Department of Electrical, Electronic, Telecommunications Engineering and Naval Architecture (DITEN), University of Genoa, 16145 Genoa, Italy (e-mail: chiara.dachena@edu.unige.it, alessandro.fedeli@unige.it, matteo.pastorino @unige.it, andrea.randazzo@unige.it).

A. Fanti is with the Department of Electrical and Electronic Engineering, University of Cagliari, 09123 Cagliari, Italy, and also with INFN-CA, Complesso Universitario di Monserrato, 09042 Cagliari, Italy (e-mail: alessandro.fanti@unica.it).

Matteo B. Lodi is with the Department of Electrical and Electronic Engineering, University of Cagliari, 09123 Cagliari, Italy, (e-mail: matteob.lodi@unica.it).

analyzed using simplified numerical models. Neck has also been considered in hyperthermia, which is widely adopted for increasing the effectiveness of radiotherapy and chemotherapy protocols [59]–[63]. The objective of hyperthermia systems is however different, since they aim to focus the electromagnetic energy in specific parts of the body. Devices like HYPERcollar [64]–[67] allow an efficient high-power (50 – 100 W) transfer into the body by using phased arrays with antennas immersed in a water bolus. Conversely, the proposed setup is specifically devoted to imaging applications, thus it requires to sequentially illuminate the whole neck to receive the scattering contributions without focusing, by also acquiring multi-frequency data to increase the available information.

In this paper, a feasibility analysis oriented toward the development of a tomographic MWI system for spinal cord diagnostics is presented. The use of MWI for this pathology is quite challenging, due to the limited attainable resolution, and constitutes the main novelty of this study. A first system prototype is reported and discussed. It is based on the acquisition of transmission measurements between antennas located all around patient's neck. Differently from typical hyperthermia systems, antennas are put very close to the neck using a custom 3D-printed structure (also supporting the coupling medium) and the working frequency is higher (600 – 900 MHz versus 434 MHz). The acquired data are processed by using a nonlinear Newton-based inverse scattering procedure [68], [69] in Lebesgue spaces, whose output is an image of the cross section of the neck. With respect to methods developed in the conventional framework of Hilbert spaces, the use of Lebesgue spaces L^p, with $p < 2$, reduce over-smoothing and ringing effects on the reconstructed dielectric profiles [69], [34]. This fact is highly beneficial for the envisioned application, in which small inclusions are searched.

The paper is organized as follows. The design of the developed imaging setup is described in Section II. The custom 3D-printed neck phantom designed for the validation phase is detailed in Section III. Numerical results and a preliminary experimental assessment are discussed in Section IV and V, respectively. Conclusions follow.

II. Design of a Microwave Imaging System for Cervical Diagnostics

In order to assess the feasibility of MWI for the diagnostic of cervical diseases, a first analysis of the electromagnetic field propagation inside a layered model of the neck has been carried out. On such basis, an initial system prototype has been devised and validated through numerical simulations and experimental measurements.

A. Field propagation in a layered model of the neck

The structure of the human neck is quite complex, since it presents several kinds of internal tissues and anatomic features. However, as in other MWI applications (e.g., brain stroke detection [70], [71]), simplified models are useful to draw initial indications about the working conditions in which the system could operate. In particular, a simplified 1D layered structure of the neck composed by five layers has been considered. The outermost semi-infinite layer, whose relative dielectric permittivity is $\epsilon_{r,b} \in [1, 80]$, represents the coupling medium outside the neck, which is used to increase the field penetration and to reduce the skin reflections that otherwise may be large. Only the real part of the dielectric permittivity has been considered, being the main parameter affecting electrical matching. Clearly, in real applications, a certain loss is present. However, it usually has a negligible impact on electrical matching [70]. The three internal layers, representing skin, fat and muscle, have thicknesses $d_{\text{skin}} = 3$ mm, $d_{\text{fat}} = 9$ mm and $d_{\text{muscle}} = 26$ mm, respectively [72]. The innermost semi-infinite layer represents the vertebral bone. The dielectric properties of these tissues have been characterized with the frequency-dependent Cole-Cole models available in [73]. This layered structure has been used to evaluate the reflection coefficient at the external interface of the neck, as well as the transmission coefficient inside the vertebral bone where the spinal canal is placed, versus the dielectric permittivity of the external matching medium and the working frequency (between 100 MHz and 3 GHz). The magnitude of these two parameters, obtained with a custom code based on the analytical formulation in [74], is shown in Fig. 1. The reflection coefficient [Fig. 1(a)] evidences a significant reflection from the skin in absence of a matching medium. However, some regions with low reflection values can be identified. The first one is located around 300 MHz, when $\epsilon_{r,b} \gtrsim 30$. The second one is between 500 MHz and 1 GHz, with a matching medium having $5 \lesssim \epsilon_{r,b} \lesssim 60$. The third one, which is partially overlapped to the second one, is between 1 GHz and 1.8 GHz and requires a matching medium with $5 \lesssim \epsilon_{r,b} \lesssim 30$. When the frequency is above 2 GHz, an important reflection appears, specifically in the absence of a matching medium. As for the transmission coefficient in Fig. 1(b), as expected higher values appear at lower frequencies in the presence of an external matching medium with $\epsilon_{r,b} \gtrsim 5$, which increases the field penetration inside the innermost layer of the model. It is worth noting that the quite low reflection coefficient around 1.1 GHz does not reflect into a corresponding peak in the transmission coefficient due to the significant losses that the considered tissues exhibit in this band, combined with the multilayer structure. On these bases, the working frequency range has been chosen as a trade-off between low reflection from skin and high transmission toward the vertebra. Consequently, the second frequency band and a matching medium with $5 \lesssim \epsilon_{r,b} \lesssim 60$ have been selected.

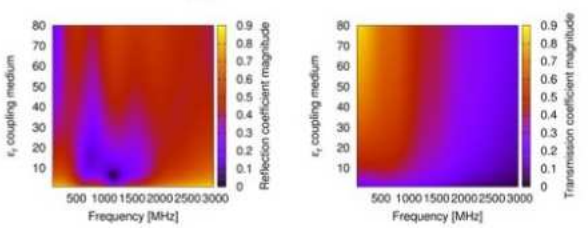

Fig. 1. (a) Reflection and (b) transmission coefficients for different values of the frequency and of the dielectric permittivity of the matching medium.

B. Structure of the Proposed Microwave Imaging System

The feasibility of MWI to detect the considered cervical disease has been assessed using an initial system prototype, built on the basis of the operating conditions defined in Section II.A. The system process the scattered-field data acquired with a vector network analyzer (VNA) by means of a nonlinear inverse-scattering technique, and provides an image of the cross section of the neck useful to estimate the dimensions of the spinal canal. The structure of the prototype is outlined in Fig. 2, where both the measurement instrumentation and the processing scheme are highlighted.

Regarding the hardware part, a two-port 8753E VNA (Keysight Technologies, Santa Rosa, CA, USA) is used for performing measurements in a multistatic arrangement, as in [34]. A single antenna radiates at a time, and all other antennas are subsequently swept to obtain multi-view data. To this end, a microwave switch matrix is connected between the VNA and antenna ports through RG047 50-Ω coaxial cables [34]. Switch matrix operations are controlled by a MATLAB R2019a (The MathWorks, Natick, MA, USA) interface through a local area network (LAN) link, whereas measurements are synchronously acquired by using a 82357A GPIB-to-USB adapter (Keysight Technologies, Santa Rosa, CA, USA). The radiating/receiving device is composed by $N_a = 10$ slotted bowtie-like antenna elements with back cavity realized on FR-4 substrate [75]. The probing elements, which work in the frequency band selected in Section II.A, are supported by a modular 3D printed assembly with the shape of a circular collar containing N_a holes where antennas are nestled. The holes have outer and inner sizes 46×26 mm and 42×21 mm, respectively, and are 8 mm deep. The assembly is composed of two equal parts hooked with two joints that allow a comfortable application on patient's neck (inner and outer radiuses are 64.5 mm and 73.5 mm, respectively, whereas height is 54 mm). The structure is made of polylactic acid (PLA) and it is 3D printed with filament size 1.75 mm, layer thickness 0.25 mm, infill density equal to 15 %, and infill velocity 80 mm/s. According to the indications obtained in Section II.A, the coupling between antennas and neck is ensured by plastic bags filled with a mixture glycerin/water with 70% volumetric content of glycerin (whose dielectric properties are reported in [34], [76] and shown in Fig. 3(a)) placed in contact with the radiating surface of each antenna. Such bags also allow to compensate for variations in neck size.

C. Outline of the Inverse Scattering Procedure

The acquired data are processed by an inverse scattering procedure for reconstructing the dielectric properties of the cross section of the neck. Let us assume a tomographic configuration and denote as R_i the region of interest with circular shape that encloses patient's neck. The objective is to retrieve the contrast function $\chi(\mathbf{r}) = \varepsilon(\mathbf{r})/\varepsilon_b - 1$, $\mathbf{r} \in R_i$, where $\varepsilon(\mathbf{r})$ and ε_b are the dielectric permittivity of the region of interest and background, respectively. Starting from χ, the properties of the spinal canal can be estimated.

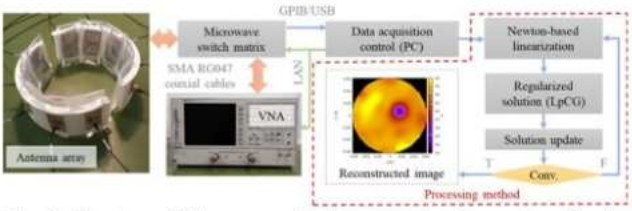

Fig. 2. Structure of the proposed microwave imaging system for the diagnosis of cervical diseases.

In order to obtain such a quantity, it is assumed to have at disposal two distinct sets of measurements at frequency f (an $e^{j2\pi ft}$ time dependence is considered and omitted). The first one is related to a reference configuration χ_{ref}, e.g., a known/partially known neck, whereas the second one refers to the actual dielectric profile χ. In a real monitoring framework, the reference profile can be obtained from other imaging modalities, e.g., MRI. Transmission measurements performed by the VNA are used to obtain an estimate of the z-component of the electric field at receiving antenna positions. Consequently, the following two sets of electric field measurements are available: $e_v^{ref}(\mathbf{r})$, $v = 1, \dots, N_a$, $\mathbf{r} \in M_v$, and $e_v(\mathbf{r})$, $v = 1, \dots, N_a$, $\mathbf{r} \in M_v$, where M_v is the measurement domain for the vth transmitting antenna. The problem unknown $u(\mathbf{r}) = \chi(\mathbf{r}) - \chi_{ref}(\mathbf{r})$, $\mathbf{r} \in R_i$, is the difference between the actual, $\chi(\mathbf{r})$, and the reference, $\chi_{ref}(\mathbf{r})$, contrast function, and is related to the electric field measurements as

$$\begin{bmatrix} e_1(\mathbf{r}) - e_1^{ref}(\mathbf{r}) \\ \vdots \\ e_{N_a}(\mathbf{r}) - e_{N_a}^{ref}(\mathbf{r}) \end{bmatrix} = \begin{bmatrix} \mathcal{G}_{M_1} u \left(I - \mathcal{G}_{R_i} u\right)^{-1} e_1^{ref}(\mathbf{r}) \\ \vdots \\ \mathcal{G}_{M_{N_a}} u \left(I - \mathcal{G}_{R_i} u\right)^{-1} e_{N_a}^{ref}(\mathbf{r}) \end{bmatrix} \quad (1)$$

where $\mathcal{G}_{M_v}$, $v = 1, \dots, N_a$, and $\mathcal{G}_{R_i}$ are defined as

$$\mathcal{G}_{\substack{M_v \\ R_i}} w(\mathbf{r}) = -k_b^2 \int_{R_i} w(\mathbf{r}') g_{ref}(\mathbf{r}, \mathbf{r}') d\mathbf{r}', \mathbf{r} \in \begin{matrix} M_v \\ R_i \end{matrix} \quad (2)$$

in which $k_b^2 = \omega^2 \mu_0 \varepsilon_b$ and whose kernel, g_{ref}, is the Green's function for the dielectric profile characterized by the reference contrast function χ_{ref} [27].

Equation (1) can be written in compact form as $\mathcal{N}(u) = y$, where $\mathcal{N}$ is a non-linear operator describing the electromagnetic scattering phenomena and y contains the measured data. Such an equation, which should be solved with respect to the unknown u, is strongly nonlinear and ill-posed. To solve it, a nonlinear inverse-scattering approach with L^p-space regularization capabilities has been applied. As outlined in Fig. 2, the inversion method is based on a Newton-type iterative loop [69], [75]. The above nonlinear equation is first linearized around the value reconstructed at the lth iteration, leading to the equation $\mathcal{N}'_{u_l}\delta = y - \mathcal{N}(u_l) \triangleq r_l$, with $\delta \in A$, $r_l \in B$, A, B being L^p spaces. The solution of this linear problem is obtained by an iterative conjugate-gradient-like approach in Lebesgue spaces (LpCG) [75]. Specifically, at the kth inner iteration, the search direction is updated as

$$d_k = -N'^{*}_{u_l} J_B\left(N'_{u_l}\delta_k - r_l\right) + \beta_k d_{k-1} \quad (3)$$

and the solution is computed as

$$\delta_{k+1} = J_{A^*}[J_A(\delta_k) + \alpha_k d_k] \quad (4)$$

where J_A, J_{A^*} and J_B are the duality maps of the corresponding L^p spaces, whose explicit formulas are reported in [77] along with the parameters α_k and β_k. The iterations are initialized with $\delta_0 = 0$ and $d_0 = N'^{*}_{u_l} J_B(r_l)$. Once the linear problem is solved, the solution is updated as $u_{l+1} = u_l + \delta$. The iterations are stopped when a predefined maximum number of iterations (L and K for the outer and inner loops, respectively) or a threshold R_{th} on the relative variations of the data residuals between two iterations are reached [69], [75]. The proposed inverse-scattering method also exploit multifrequency data by using a frequency-hopping approach, where the solutions obtained at lower frequencies are used to initialize the inversion algorithm at the following frequency steps [27].

III. Neck Phantoms

The feasibility of the diagnostic system in Section II has been numerically and experimentally assessed with simplified phantoms of the neck. To the best of authors' knowledge, 3D printed neck phantoms for MWI are not available in the scientific literature. Indeed, numerical neck phantoms were mainly used for hyperthermia treatments [78] or to evaluate the SAR distribution in semi-deep hyperthermia [72]. Realistic head phantoms have been developed for MWI [79], [80], but without the neck. For this reason, a simplified neck phantom was specifically designed and developed. The geometry of the phantom, which has been designed on the basis of the geometrical shape reported in [72] and by using the average dimensions in [48], is shown in Fig. 4. It consists of a plastic cylinder with an internal circular inclusion close to the outer border that represents the trachea. The outer boundary has a circular cross section with diameter $d_{out} = 110$ mm and height $h_n = 110$ mm. Internally, a circular compartment with diameter $d_{in} = 95$ mm was created with center at $(-1.75,0)$ mm. The trachea has inner and outer diameters $d_{in/t} = 18$ mm and $d_{out/t} = 24$ mm, respectively, both with center at $(-39.5,0)$ mm. Inclusions of different sizes and complexity can be placed inside this structure for modeling the spinal canal and/or the vertebral column. In this way, it is possible to simulate different neck conditions by exchanging the removable parts.

A first model ("Phantom 1") includes liquid-filled glass tubes [Fig. 4(a)] to simulate different sizes of the spinal canal. Two tubes have been tested, with inner diameters $d_t = 24$ mm and $d_t = 10$ mm. An improved model includes a 3D-printed simplified section of the vertebral column ("Phantom 2"). The shape of this part is sketched in Fig. 4(g), and the corresponding dimensions are $r_1 = 42.3$ mm, $r_2 = 43.1$ mm, $r_3 = 13$ mm, $a_1 = 48$ mm, $a_2 = 39$ mm, $a_3 = 6$ mm, and $a_4 = 3$ mm. The spinal canal inclusion has an inner diameter $d_{sc} = 18$ mm and it is centered at (5,0) mm. This block has a thickness of 2 mm to allow its physical stability. Despite their simplicity, the adopted structures contain many anatomical details that introduce significant difficulties in a real applicative scenario (such as the trachea, containing air, and the high contrast bone parts). Moreover, since different canal sizes can be used, it is possible to evaluate the reconstruction capabilities in a controlled environment.

As a preliminary proof of concept, the phantoms have been filled with glycerin/water mixtures in different concentrations to approximate the average contrast between neck tissues. In particular, a glycerin/water mixture with 70% volumetric content of glycerin has been used to fill the main structure. The spinal canal has been modelled with a 80% glycerin/water mixture, whereas pure glycerin has been used for the vertebral bone. The presence of plastic/glass layers has a tolerable impact on the transmitted microwave signals and causes a small difference (about 1.3% on the total field measured in the location opposite to the source, as verified by numerical simulations). The dielectric properties of the involved liquids have been obtained by means of reflection coefficient measurements on a liquid-filled section of a short-circuited coaxial line [81]. Table I reports the parameters of the single pole Debye models obtained by fitting the measured data. As shown in Fig. 3(a), the relative dielectric permittivity of the adopted mixtures are quite similar to those of the corresponding biological tissues (on the basis of [82], [83], average neck properties are calculated with a concentration of 80% muscle and 20% fat). Fig. 3(b) reports the simulated and actual contrasts between spinal cord and bone (blue line) and between spinal cord and average neck (green line), which also show a good agreement. PLA was used to create the main structure; it is also used as a supporting material for trachea and internal inclusions. The dielectric properties of PLA reported in [84] have been considered in this work.

IV. Numerical Results

The suitability of the nonlinear inverse-scattering method adopted for processing the measured data has been initially tested by means of numerical simulations involving numerical models that reproduce the 3D printed phantoms shown in Fig. 4(a) and Fig. 4(b). First, the simplified neck model "Phantom 1" was considered. The dielectric properties of the simulated phantoms have been characterized by using the Debye model reported in Table I.

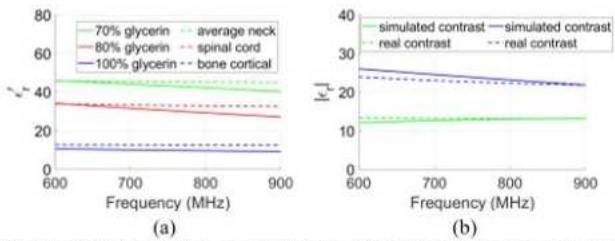

Fig. 3. (a) Relative dielectric permittivity of biological tissues and glycerin in different concentrations. (b) Real and simulated dielectric contrast between spinal cord and bone and between spinal cord and average neck.

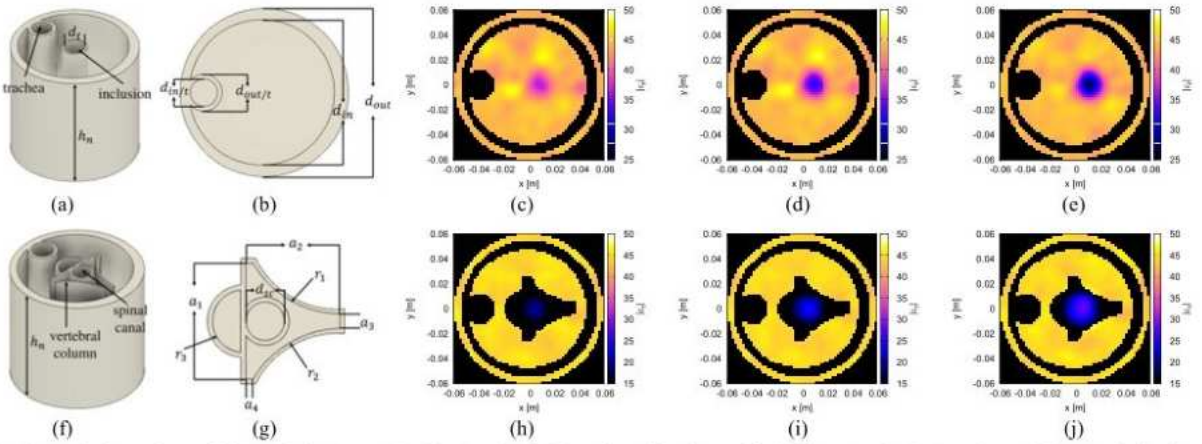

Fig. 4. Design and dimensions of the neck phantoms: (a) Phantom 1; (b) Top view of neck model; (f) Phantom 2; (g) Top view of the vertebral column model. Reconstructed relative dielectric permittivity: Phantom 1: (c) 14 mm, (d) 18 mm, (e) 24 mm. Phantom 2: (h) 14 mm, (i) 18 mm, (j) 24 mm.

TABLE I
PARAMETERS OF THE FIRST-ORDER DEBYE MODELS OF THE GLYCERIN/WATER MIXTURES USED INSIDE THE NECK PHANTOM.

Tissue	Glycerin (vol.)	ε_∞	$\Delta\varepsilon_1$	τ_1 [ps]	σ_s [mS/m]
Avg. neck	70%	12.440	40.157	116.75	127.46
Spinal cord	80%	10.999	35.360	192.48	135.16
Bone	100%	5.7649	7.1352	187.52	219.74

The outer layer (matching medium) has thickness 5 mm and is filled with 70% glycerin/water mixture. The PLA parts have been modeled with relative dielectric permittivity $\varepsilon_r = 3$ and electric conductivity $\sigma = 0.001$ S/m. According to Section II.B, $N_a = 10$ antennas uniformly spaced on a circumference of diameter $d = 128$ mm has been used. Each antenna (modeled as a line-current source) acts in turn in transmission mode and the remaining $M = N_a - 1$ positions are used to collect the scattered electric field data. A 2-D simulator based on method of moments has been used for performing the forward simulations [85]. Frequency-domain data between 600 and 900 MHz with 50 MHz frequency step have been considered. The investigation domain R_i is a circular region located on the horizontal plane with diameter equal to 120 mm and discretized with $N_f = 11304$ square cells of side 1 mm. A white Gaussian noise with zero mean value and variance corresponding to a signal-to-noise ratio (SNR) of 35 dB (i.e., comparable to noise from a realistic measurement system [86]) has been added to the total electric field data. In the inversion procedure, the investigation domain has been partitioned into $N_{inv} = 2828$ square cells of side 2 mm, and the following parameters have been heuristically chosen: $p = 1.4$, $L = 20$, $K = 10$, $R_{th} = 0.01$. The reference scenario has been assumed to be the actual neck without the spinal canal.

Three different diameters of the spinal canal have been considered: 14 mm (i.e., comparable to a pathological condition), 18 mm, and 24 mm. The reconstructed dielectric properties at 900 MHz are shown in Fig. 4(c), Fig. 4(d) and Fig. 4(e), respectively. The estimated diameters of the spinal cord (a threshold equal to 45% of the contrast between spinal cord and average neck has been used) are 16.6 mm, 21.9 mm, and 25.8 mm, respectively. Such values are very close to the actual ones and allow distinguishing between the different canal sizes. The method requires for each frequency an average number of 3 outer iterations to converge and the corresponding computational time is 92 seconds on a PC equipped with an Intel® Core™ i7-2600K @ 3.4 GHz processor and 8 GB of RAM.

As a second test case, the more complex "Phantom 2" [Fig. 4(f)], containing the simplified vertebral column model, has been considered. Similar to the previous simulated cases, the three diameters 14 mm, 18 mm and 24 mm of the spinal canal inside the vertebral column have been considered. All the other parameters are the same as in the previous case. The reference scenario is the actual neck with the vertebra bone and without the spinal canal (in real applications such a profile may be obtained from previous MRI or CT images). The reconstructed dielectric profiles are reported in Fig. 4(h), Fig. 4(i), and Fig. 4(j). In this case, the estimated diameters are 15.8 mm, 22.7 mm, and 28.8 mm, which again allow distinguishing the pathologic condition from the normal ones.

V. EXPERIMENTAL RESULTS

Some preliminary experimental results are presented in this Section. Initially, the MWI system has been tested using the simplified phantom shown in Fig. 5(a), composed of a circular glass beaker with external diameter $d_b = 107$ mm filled with a 70 % glycerin/water mixture (simulating the average dielectric properties of internal neck tissues). Circular inclusions filled with an 80% glycerin/water mixture have been placed inside the beaker to simulate the spinal canal. The system described in Section II.B has been used to collect data between 600 and 900 MHz with 50 MHz frequency step. The reference configuration is a homogenous cylinder with the dielectric properties of a 70% glycerin/water mixture.

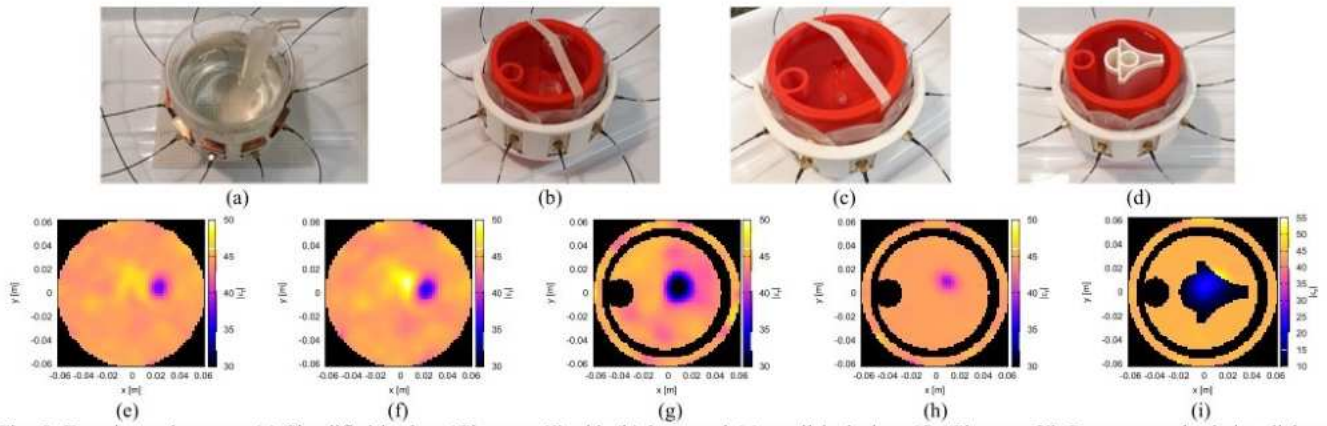

Fig. 5. Experimental targets: (a) Simplified beaker; "Phantom 1" with (b) large and (c) small inclusion; (d) "Phantom 2". Reconstructed relative dielectric permittivity: (e) Simplified beaker with (e) small and (f) middle-size inclusion; "Phantom 1" with (g) large and (h) small inclusion; (i) "Phantom 2".

Before measurements, a full reflection/transmission 2-port calibration of the VNA has been performed by considering the antennas located on the opposite sides of the target and using the 85033A SMA 50Ω calibration kit (Keysight Technologies, Santa Rosa, CA, USA). The reference configuration has been used to match the measured values with the simulated ones, in order to properly scale the internal electric field. The region of interest R_i (which coincides with a horizontal cross section of the neck phantom) has a diameter of 122 mm and is partitioned into $N_{inv} = 3024$ square cells of side 2 mm. The following parameters have been used: $p = 1.4$, $L = 20$, $K = 10$, $R_{th} = 0.1$. Two different diameters of the inclusion modeling the spinal canal have been considered: $d_g = 12.4$ mm and $d_p = 16.9$ mm. The reconstructed dielectric properties are shown in Fig. 5(e) and Fig. 5(f), respectively. In both cases, the internal cylindrical inclusion is characterized correctly. The estimated diameters are 10.3 mm and 15.8 mm, respectively.

Subsequently, the imaging setup has been tested with the 3D printed neck phantom. Initially, the simplified structure "Phantom 1" has been adopted. As shown in Fig. 5(b) and Fig. 5(c), two different diameters of the inclusions, i.e., $d_g = 24$ mm and $d_g = 10$ mm, have been considered. The investigation domain has a diameter of 124 mm and it is partitioned into $N_{inv} = 5024$ square cells of side length equal to 1.5 mm. The printed phantom without inclusions has been used as reference model and the inversion parameters for the first dimension are: $p = 1.4$, $L = 20$, $K = 10$, $R_{th} = 0.2$. For the second case, $p = 1.2$ whereas the other parameters are the same. The reconstructed dielectric properties are shown in Fig. 5(g) and Fig. 5(h), respectively. The sizes of the inclusion are quite correctly identified in both cases (the estimated diameters are 27.4 mm and 7.2 mm, respectively), confirming that even when using a more complex host structure, it is still possible to distinguish between the two different sizes.

The last considered configuration is based on the more accurate "Phantom 2", as shown in Fig. 5(d). The bone-related sections are filled with pure glycerin and the internal inclusion is filled with a 80 % glycerin/water mixture to simulate the spinal canal, which has a diameter of 18 mm. The investigation domain is the same used in the previous cases and the considered reference scenario is a numerical model of the phantom with the vertebral-mimicking section filled with pure glycerin. It is worth noting that in this case, the reference configuration is not exact since the PLA boundaries are not included in the numerical model. The inversion parameters are the same as before. The reconstructed dielectric properties are reported in Fig. 5(i). Although the increased complexity of this phantom leads to a slight decrease in reconstruction accuracy (the estimated diameter is 22.5 mm), it confirms the possibility of identifying the inclusion even in this more challenging case.

VI. Conclusion

A feasibility analysis devoted to the development of an imaging system working at microwave frequencies for spinal cord diagnostics has been proposed. A preliminary prototype has been described. It is based on the use of a set of antennas that can be positioned around patient's neck. The samples of the measured scattered electric field are used to reconstruct two-dimensional images of the neck by solving the related inverse scattering problem. To perform this task, an efficient nonlinear Newton-based method has been applied. Numerical results have been reported and discussed. Moreover, some experimental reconstructions performed by using a 3D printed neck phantom have also been included. Although preliminary, these results seem to indicate the potentialities of MWI techniques in detecting significant changes in the spinal cord size, which may be symptoms of cervical myelopathy. Indeed, the diameters estimated from the retrieved images seem to allow discriminating between the normal and pathologic conditions. Further developments will be devoted to further improve the proposed initial prototype and to evaluate its applicability to more realistic models of the human neck. Moreover, the application to real human subjects will be also considered, in order to further validate the capabilities of the approach. Finally, the possibility of using existing hyperthermia setups for the microwave imaging of the cervical region will be explored, too.

REFERENCES

[1] L. E. Larsen and J. H. Jacobi, Eds., *Medical applications of microwave imaging*. New York: IEEE Press, 1985.

[2] A. Benedetto and L. Pajewski, *Civil Engineering Applications of Ground Penetrating Radar*. Cham: Springer, 2015.

[3] I. Giannakis, F. Tosti, L. Lantini, and A. M. Alani, 'Diagnosing Emerging Infectious Diseases of Trees Using Ground Penetrating Radar', *IEEE Trans. Geosci. Remote Sens.*, vol. 58, no. 2, pp. 1146–1155, Feb. 2020.

[4] F. Boero, A. Fedeli, M. Lanini, M. Maffongelli, R. Monleone, M. Pastorino, *et al.*, 'Microwave tomography for the inspection of wood materials: imaging system and experimental results', *IEEE Trans. Microw. Theory Techn.*, pp. 1–14, 2018.

[5] J. Laviada, B. Wu, M. T. Ghasr, and R. Zoughi, 'Nondestructive Evaluation of Microwave-Penetrable Pipes by Synthetic Aperture Imaging Enhanced by Full-Wave Field Propagation Model', *IEEE Trans. Instrum. Meas.*, vol. 68, no. 4, pp. 1112–1119, Apr. 2019.

[6] G. Bozza, C. Estatico, A. Massa, M. Pastorino, and A. Randazzo, 'Short-range image-based method for the inspection of strong scatterers using microwaves', *IEEE Trans. Instrum. Meas.*, vol. 56, no. 4, pp. 1181–1188, Aug. 2007.

[7] S. Pisa, E. Piuzzi, E. Pittella, P. D'Atanasio, A. Zambotti, and G. Sacco, 'Comparison between delay and sum and range migration algorithms for image reconstruction in through-the-wall radar imaging systems', *IEEE J. Electromagn. RF Microw. Med. Biol.*, vol. 2, no. 4, pp. 270–276, Dec. 2018.

[8] J.-C. Bolomey, 'Advancing Microwave-Based Imaging Techniques for Medical Applications in the Wake of the 5G Revolution', in *Proc. 13th Eur. Conf. Antennas Propag.*, Krakow, Poland, 2019, pp. 1–5.

[9] W. Shao and T. McCollough, 'Advances in Microwave Near-Field Imaging: Prototypes, Systems, and Applications', *IEEE Microw. Mag.*, vol. 21, no. 5, pp. 94–119, May 2020.

[10] M. A. Aldhaeebi, K. Alzoubi, T. S. Almoneef, S. M. Bamatraf, H. Attia, and O. M. Ramahi, 'Review of Microwaves Techniques for Breast Cancer Detection', *Sensors*, vol. 20, no. 8, p. 2390, Jan. 2020.

[11] R. Chandra, H. Zhou, I. Balasingham, and R. M. Narayanan, 'On the Opportunities and Challenges in Microwave Medical Sensing and Imaging', *IEEE Trans. Biomed. Eng.*, vol. 62, no. 7, pp. 1667–1682, Jul. 2015.

[12] S. Semenov, 'Microwave tomography: review of the progress towards clinical applications', *Philos. Transact. A Math. Phys. Eng. Sci.*, vol. 367, no. 1900, pp. 3021–3042, Aug. 2009.

[13] H. A. Lumley, D. Flynn, L. Shaw, G. McClelland, G. A. Ford, P. M. White, *et al.*, 'A scoping review of pre-hospital technology to assist ambulance personnel with patient diagnosis or stratification during the emergency assessment of suspected stroke', *BMC Emerg. Med.*, vol. 20, no. 1, p. 30, Apr. 2020.

[14] D. Tajik, F. Foroutan, D. S. Shumakov, A. D. Pitcher, and N. K. Nikolova, 'Real-time microwave imaging of a compressed breast phantom with planar scanning', *IEEE J. Electromagn. RF Microw. Med. Biol.*, vol. 2, no. 3, pp. 154–162, Sep. 2018.

[15] A. Abubakar, P. M. van den Berg, and J. J. Mallorqui, 'Imaging of biomedical data using a multiplicative regularized contrast source inversion method', *IEEE Trans. Microw. Theory Techn.*, vol. 50, no. 7, pp. 1761–1771, Jul. 2002.

[16] T. Henriksson, N. Joachimowicz, C. Conessa, and J.-C. Bolomey, 'Quantitative microwave imaging for breast cancer detection using a planar 2.45 GHz system', *IEEE Trans. Instrum. Meas.*, vol. 59, no. 10, pp. 2691–2699, Oct. 2010.

[17] Z. Miao and P. Kosmas, 'Multiple-frequency DBIM-TwIST algorithm for microwave breast imaging', *IEEE Trans. Antennas Propag.*, vol. 65, no. 5, pp. 2507–2516, May 2017.

[18] G. Bellizzi, G. G. Bellizzi, O. M. Bucci, L. Crocco, M. Helbig, S. Ley, *et al.*, 'Optimization of the working conditions for magnetic Nanoparticle-enhanced microwave diagnostics of breast cancer', *IEEE Trans. Biomed. Eng.*, vol. 65, no. 7, pp. 1607–1616, Jul. 2018.

[19] L. M. Neira, B. D. Van Veen, and S. C. Hagness, 'High-resolution microwave breast imaging using a 3-D inverse scattering algorithm with a variable-strength spatial prior constraint', *IEEE Trans. Antennas Propag.*, vol. 65, no. 11, pp. 6002–6014, Nov. 2017.

[20] S. Di Meo, P. F. Espin-Lopez, A. Martellosio, M. Pasian, G. Matrone, M. Bozzi, *et al.*, 'On the feasibility of breast cancer imaging systems at millimeter-waves frequencies', *IEEE Trans. Microw. Theory Techn.*, vol. 65, no. 5, pp. 1795–1806, May 2017.

[21] M. Ambrosanio, P. Kosmas, and V. Pascazio, 'A multithreshold iterative DBIM-based algorithm for the imaging of heterogeneous breast tissues', *IEEE Trans. Biomed. Eng.*, vol. 66, no. 2, pp. 509–520, Feb. 2019.

[22] G. Boverman, C. E. L. Davis, S. D. Geimer, and P. M. Meaney, 'Image registration for microwave tomography of the breast using priors from nonsimultaneous previous magnetic resonance images', *IEEE J. Electromagn. RF Microw. Med. Biol.*, vol. 2, no. 1, pp. 2–9, Mar. 2018.

[23] M. Asefi, A. Zakaria, and J. LoVetri, 'Microwave imaging using normal electric-field components inside metallic resonant chambers', *IEEE Trans. Microw. Theory Techn.*, vol. 65, no. 3, pp. 923–933, Mar. 2017.

[24] H. Trefna and M. Persson, 'Antenna array design for brain monitoring', in *Proc. 2008 IEEE Antennas Propag. Soc. Int. Symp.*, San Diego, CA, USA, 2008, pp. 1–4.

[25] S. Y. Semenov and D. R. Corfield, 'Microwave tomography for brain imaging: Feasibility assessment for stroke detection', *Int. J. Antennas Propag.*, vol. 2008, Art. ID 254830, May 2008.

[26] L. Crocco, I. Karanasiou, M. James, and R. C. Conceição, *Emerging Electromagnetic Technologies for Brain Diseases Diagnostics, Monitoring and Therapy*. Cham, Switzerland: Springer, 2018.

[27] M. Pastorino and A. Randazzo, *Microwave Imaging Methods and Applications*. Boston, MA: Artech House, 2018.

[28] V. L. Coli, P.-H. Tournier, V. Dolean, I. E. Kanfoud, C. Pichot, C. Migliaccio, *et al.*, 'Detection of simulated brain strokes using microwave tomography', *IEEE J. Electromagn. RF Microw. Med. Biol.*, vol. 3, no. 4, pp. 254–260, Dec. 2019.

[29] A. Afsari, A. M. Abbosh, and Y. Rahmat-Samii, 'Modified Born iterative method in medical electromagnetic tomography using magnetic field fluctuation contrast source operator', *IEEE Trans. Microw. Theory Techn.*, vol. 67, no. 1, pp. 454–463, Jan. 2019.

[30] J. A. Tobon Vasquez, R. Scapaticci, G. Turvani, G. Bellizzi, N. Joachimowicz, B. Duchêne, *et al.*, 'Design and experimental assessment of a 2D microwave imaging system for brain stroke monitoring', *Int. J. Antennas Propag.*, vol. 2019, Article ID 8065036, 2019.

[31] R. Scapaticci, J. Tobon, G. Bellizzi, F. Vipiana, and L. Crocco, 'Design and numerical characterization of a low-complexity microwave device for brain stroke monitoring', *IEEE Trans. Antennas Propag.*, vol. 66, no. 12, pp. 7328–7338, Dec. 2018.

[32] M. Salucci, A. Gelmini, J. Vrba, I. Merunka, G. Oliveri, and P. Rocca, 'Instantaneous brain stroke classification and localization from real scattering data', *Microw. Opt. Technol. Lett.*, vol. 61, no. 3, pp. 805–808, 2019.

[33] A. E. Stancombe, K. S. Bialkowski, and A. M. Abbosh, 'Portable microwave head imaging system using software-defined radio and switching network', *IEEE J. Electromagn. RF Microw. Med. Biol.*, vol. 3, no. 4, pp. 284–291, Dec. 2019.

[34] I. Bisio, C. Estatico, A. Fedeli, F. Lavagetto, M. Pastorino, A. Randazzo, *et al.*, 'Variable-exponent Lebesgue-space inversion for brain stroke microwave imaging', *IEEE Trans. Microw. Theory Techn.*, vol. 68, no. 5, pp. 1882–1895, May 2020.

[35] P.-H. Tournier, M. Bonazzoli, V. Dolean, F. Rapetti, F. Hecht, F. Nataf, *et al.*, 'Numerical modeling and high-speed parallel computing: New perspectives on tomographic microwave imaging for brain stroke detection and monitoring', *IEEE Antennas Propag. Mag.*, vol. 59, no. 5, pp. 98–110, Oct. 2017.

[36] P. M. Meaney, M. W. Fanning, D. Li, S. P. Poplack, and K. D. Paulsen, 'A clinical prototype for active microwave imaging of the breast', *IEEE Trans. Microw. Theory Techn.*, vol. 48, no. 11, pp. 1841–1853, Nov. 2000.

[37] N. R. Epstein, P. M. Meaney, and K. D. Paulsen, '3D parallel-detection microwave tomography for clinical breast imaging', *Rev. Sci. Instrum.*, vol. 85, no. 12, Dec. 2014.

[38] J. Ljungqvist, S. Candefjord, M. Persson, L. Jönsson, T. Skoglund, and M. Elam, 'Clinical Evaluation of a Microwave-Based Device for Detection of Traumatic Intracranial Hemorrhage', *J. Neurotrauma*, vol. 34, no. 13, pp. 2176–2182, Feb. 2017.

[39] J. S. Hudson, T. K. Chung, B. S. Prout, Y. Nagahama, M. L. Raghavan, and D. M. Hasan, 'Iron nanoparticle contrast enhanced microwave imaging for emergent stroke: A pilot study', *J. Clin. Neurosci.*, vol. 59, pp. 284–290, Jan. 2019.

[40] L. Sani, N. Ghavami, A. Vispa, M. Paoli, G. Raspa, M. Ghavami, *et al.*, 'Novel microwave apparatus for breast lesions detection: Preliminary clinical results', *Biomed. Signal Process. Control*, vol. 52, pp. 257–263, Jul. 2019.

[41] A. Zakaria, A. Baran, and J. LoVetri, 'Estimation and Use of Prior Information in FEM-CSI for Biomedical Microwave Tomography', *IEEE Antennas Wirel. Propag. Lett.*, vol. 11, pp. 1606–1609, 2012.

[42] D. Gibbins, D. Byrne, T. Henriksson, B. Monsalve, and I. J. Craddock, 'Less Becomes More for Microwave Imaging: Design and Validation of an Ultrawide-Band Measurement Array.', *IEEE Antennas Propag. Mag.*, vol. 59, no. 5, pp. 72–85, Oct. 2017.

[43] A. Darvazehban, S. Ahdi Rezaeieh, A. Zamani, and A. M. Abbosh, 'Pattern Reconfigurable Metasurface Antenna for Electromagnetic Torso Imaging', *IEEE Trans. Antennas Propag.*, vol. 67, no. 8, pp. 5453–5462, Aug. 2019.

[44] P. M. Meaney, D. Goodwin, A. H. Golnabi, T. Zhou, M. Pallone, S. D. Geimer, *et al.*, 'Clinical Microwave Tomographic Imaging of the Calcaneus: A First-in-Human Case Study of Two Subjects', *IEEE Trans. Biomed. Eng.*, vol. 59, no. 12, pp. 3304–3313, Dec. 2012.

[45] S. K. Karadimas, G. Gatzounis, and M. G. Fehlings, 'Pathobiology of cervical spondylotic myelopathy', *Eur. Spine J.*, vol. 24, no. 2, pp. 132–138, Apr. 2015.

[46] R. Rao, 'Neck Pain, Cervical Radiculopathy, and Cervical Myelopathy: Pathophysiology, Natural History, and Clinical Evaluation', *JBJS*, vol. 84, no. 10, pp. 1872–1881, Oct. 2002.

[47] C. de O. Vilaça, M. Orsini, M. A. A. Leite, M. R. G. de Freitas, E. Davidovich, R. Fiorelli, *et al.*, 'Cervical spondylotic myelopathy: What the neurologist should know', *Neurol. Int.*, vol. 8, no. 4, Nov. 2016.

[48] G. D. Cramer and S. A. Darby, *Clinical Anatomy of the Spine, Spinal Cord, and ANS*, Third Edition. Elsevier Health Sciences, 2017.

[49] E. Baron and W. Young, 'Cervical spondylotic myelopathy: A brief review of its pathophysiology, clinical course, and diagnosis', *Neurosurgery*, vol. 60, no. 1, Jan. 2007.

[50] J. G. Arnold, 'The clinical manifestations of spondylochondrosis (spondylosis) of the cervical spine', *Ann. Surg.*, vol. 141, no. 6, pp. 872–889, Jun. 1955.

[51] A. L. Hillman and J. S. Schwartz, 'The Adoption and Diffusion of CT and MRI in the United States: A Comparative Analysis', *Med. Care*, vol. 23, no. 11, p. 1283, Nov. 1985.

[52] M. J. Callahan, R. D. MacDougall, S. D. Bixby, S. D. Voss, R. L. Robertson, and J. P. Cravero, 'Ionizing radiation from computed tomography versus anesthesia for magnetic resonance imaging in infants and children: patient safety considerations', *Pediatr. Radiol.*, vol. 48, no. 1, pp. 21–30, Jan. 2018.

[53] R. A. Bell, 'Economics of MRI technology', *J. Magn. Reson. Imaging JMRI*, vol. 6, no. 1, pp. 10–25, Feb. 1996.

[54] J. C. Robinson, C. Whaley, and T. T. Brown, 'Reference Pricing, Consumer Cost-Sharing, and Insurer Spending for Advanced Imaging Tests', *Med. Care*, vol. 54, no. 12, pp. 1050–1055, Dec. 2016.

[55] M. T. Islam, M. Z. Mahmud, M. T. Islam, S. Kibria, and M. Samsuzzaman, 'A Low Cost and Portable Microwave Imaging System for Breast Tumor Detection Using UWB Directional Antenna array', *Sci. Rep.*, vol. 9, no. 1, p. 15491, Oct. 2019.

[56] T. C. Guo and W. W. Guo, 'High resolution microwave imaging simulation of a human neck', in *Proc. 16th IEEE Instrum. Meas. Technol. Conf.*, Venice, Italy, 1999, pp. 1586–1590.

[57] G. Pagana, E. Lepore, N. Pugno, E. A. Attardo, and G. Vecchi, 'Microwave imaging: From soft towards hard tissue monitoring', in *Proc. 2nd Int. Symp. Appl. Sci. Biomed. Commun. Technol.*, Bratislava, Slovakia, 2009, pp. 1–5.

[58] S. A. Muqatash, M. Khamechi, and A. Sabouni, 'Detection of the cervical spondylotic myelopathy using noninvasive microwave imaging technique', in *Proc 2017 IEEE Int. Symp. Antennas Propag. Usn. Natl. Radio Sci. Meet.*, San Diego, CA, USA, 2017, pp. 783–784.

[59] N. R. Datta, S. Rogers, S. G. Ordóñez, E. Puric, and S. Bodis, 'Hyperthermia and radiotherapy in the management of head and neck cancers: A systematic review and meta-analysis', *Int. J. Hyperthermia*, vol. 32, no. 1, pp. 31–40, Jan. 2016.

[60] S. Gao, M. Zheng, X. Ren, Y. Tang, and X. Liang, 'Local hyperthermia in head and neck cancer: mechanism, application and advance', *Oncotarget*, vol. 7, no. 35, pp. 57367–57378, Jun. 2016.

[61] H. D. Trefná, H. Crezee, M. Schmidt, D. Marder, U. Lamprecht, M. Ehmann, *et al.*, 'Quality assurance guidelines for superficial hyperthermia clinical trials: I. Clinical requirements', *Int. J. Hyperthermia*, vol. 33, no. 4, pp. 471–482, May 2017.

[62] H. Dobšíček Trefná, J. Crezee, M. Schmidt, D. Marder, U. Lamprecht, M. Ehmann, *et al.*, 'Quality assurance guidelines for superficial hyperthermia clinical trials : II. Technical requirements for heating devices', *Strahlenther. Onkol.*, vol. 193, no. 5, pp. 351–366, May 2017.

[63] H. P. Kok and J. Crezee, 'Hyperthermia treatment planning: clinical application and ongoing research', in *Proc. 14th Eur. Conf. Antennas Propag.*, Copenhagen, Denmark, 2020, pp. 1–5.

[64] M. M. Paulides, J. F. Bakker, E. Neufeld, J. van der Zee, P. P. Jansen, P. C. Levendag, *et al.*, 'The HYPERcollar: A novel applicator for hyperthermia in the head and neck', *Int. J. Hyperthermia*, vol. 23, no. 7, pp. 567–576, Jan. 2007.

[65] P. Togni, Z. Rijnen, W. C. M. Numan, R. F. Verhaart, J. F. Bakker, G. C. van Rhoon, *et al.*, 'Electromagnetic redesign of the HYPERcollar applicator: toward improved deep local head-and-neck hyperthermia', *Phys. Med. Biol.*, vol. 58, no. 17, p. 5997, Aug. 2013.

[66] M. M. Paulides, J. F. Bakker, N. Chavannes, and G. C. Van Rhoon, 'A Patch Antenna Design for Application in a Phased-Array Head and Neck Hyperthermia Applicator', *IEEE Trans. Biomed. Eng.*, vol. 54, no. 11, pp. 2057–2063, Nov. 2007.

[67] M. M. Paulides, R. M. C. Mestrom, G. Salim, B. B. Adela, W. C. M. Numan, T. Drizdal, *et al.*, 'A printed Yagi–Uda antenna for application in magnetic resonance thermometry guided microwave hyperthermia applicators', *Phys. Med. Biol.*, vol. 62, no. 5, pp. 1831–1847, Feb. 2017.

[68] C. Estatico, A. Fedeli, M. Pastorino, and A. Randazzo, 'A multifrequency inexact-Newton method in Lp Banach spaces for buried objects detection', *IEEE Trans. Antennas Propag.*, vol. 63, no. 9, pp. 4198–4204, Sep. 2015.

[69] C. Estatico, A. Fedeli, M. Pastorino, and A. Randazzo, 'Microwave imaging by means of Lebesgue-space inversion: An overview', *Electronics*, vol. 8, no. 9, p. 945, Sep. 2019.

[70] R. Scapaticci, L. Di Donato, I. Catapano, and L. Crocco, 'A Feasibility Study on Microwave Imaging for Brain Stroke Monitoring', *Prog. Electromagn. Res. B*, vol. 40, pp. 305–324, 2012.

[71] I. Bisio, A. Fedeli, F. Lavagetto, M. Pastorino, A. Randazzo, A. Sciarrone, *et al.*, 'A numerical study concerning brain stroke detection by microwave imaging systems', *Multimed. Tools Appl.*, vol. 77, no. 8, pp. 9341–9363, Apr. 2018.

[72] M. M. Paulides, D. H. M. Wielheesen, J. Van Der Zee, and G. C. Van Rhoon, 'Assessment of the local SAR distortion by major anatomical structures in a cylindrical neck phantom', *Int. J. Hyperthermia*, vol. 21, no. 2, pp. 125–140, Mar. 2005.

[73] S. Gabriel, R. W. Lau, and C. Gabriel, 'The dielectric properties of biological tissues: III. Parametric models for the dielectric spectrum of tissues', *Phys. Med. Biol.*, vol. 41, no. 11, pp. 2271–2293, Nov. 1996.

[74] W. C. Chew, *Waves and Fields in Inhomogeneous Media*. Piscataway, NY: IEEE Press, 1995.

[75] I. Bisio, C. Estatico, A. Fedeli, F. Lavagetto, M. Pastorino, A. Randazzo, *et al.*, 'Brain stroke microwave imaging by means of a Newton-conjugate-gradient method in Lp Banach spaces', *IEEE Trans. Microw. Theory Techn.*, vol. 66, no. 8, pp. 3668–3682, Aug. 2018.

[76] P. M. Meaney, C. J. Fox, S. D. Geimer, and K. D. Paulsen, 'Electrical characterization of glycerin: water mixtures: Implications for use as a coupling medium in microwave tomography', *IEEE Trans. Microw. Theory Techn.*, vol. 65, no. 5, pp. 1471–1478, May 2017.

[77] C. Estatico, S. Gratton, F. Lenti, and D. Titley-Peloquin, 'A conjugate gradient like method for p-norm minimization in

functional spaces', *Numer. Math.*, vol. 137, no. 4, pp. 895–922, Dec. 2017.
[78] I. Merunka, O. Fiser, L. Vojackova, J. Vrba, and D. Vrba, 'Array of balanced antipodal Vivaldi antennas used for microwave hypertermia treatment of neck cancer', in *2014 24th Int. Conf. Radioelektron.*, 2014, pp. 1–4.
[79] B. J. Mohammed, A. M. Abbosh, S. Mustafa, and D. Ireland, 'Microwave System for Head Imaging', *IEEE Trans. Instrum. Meas.*, vol. 63, no. 1, pp. 117–123, Jan. 2014.
[80] J. Lee, J. Bang, and J. Choi, 'Realistic Head Phantom for Evaluation of Brain Stroke Localization Methods Using 3D Printer', *J. Electromagn. Eng. Sci.*, vol. 16, no. 4, pp. 254–258, Oct. 2016.
[81] J. R. Baker-Jarvis, M. D. Janezic, J. H. G. Jr, and R. G. Geyer, 'Transmission/reflection and short-circuit line methods for measuring permittivity and permeability', *Tech. Note NIST TN - 1355*, vol. 1355, Jan. 1992.
[82] A. T. Whittle, I. Marshall, I. L. Mortimore, P. K. Wraith, R. J. Sellar, and N. J. Douglas, 'Neck soft tissue and fat distribution: comparison between normal men and women by magnetic resonance imaging', *Thorax*, vol. 54, no. 4, pp. 323–328, Apr. 1999.
[83] L. K. Kamibayashi and F. J. R. Richmond, 'Morphometry of Human Neck Muscles', *Spine*, vol. 23, no. 12, pp. 1314–1323, Jun. 1998.
[84] C. Dichtl, P. Sippel, and S. Krohns, 'Dielectric Properties of 3D Printed Polylactic Acid', *Adv. Mater. Sci. Eng.*, 2017.
[85] J. Richmond, 'Scattering by a dielectric cylinder of arbitrary cross section shape', *IEEE Trans. Antennas Propag.*, vol. 13, no. 3, pp. 334–341, May 1965.
[86] N. K. Nikolova, *Introduction to Microwave Imaging*. Cambridge: Cambridge University Press, 2017.

Chiara Dachena received the bachelor's degree in biomedical engineering from the University of Cagliari, Cagliari, in 2017, and the master's degree in bioengineering from University of Genoa, Genoa, Italy, in 2019. She is currently working toward the Ph.D. degree in science and technology for electronic and telecommunications engineering at the University of Genoa. Her research activity deals with microwave imaging for biomedical applications; inversion procedure of scattering problems; application of machine learning for electromagnetic problems.

Alessandro Fedeli (Member, IEEE) received the B.Sc. and M.Sc. degrees in electronic engineering and the Ph.D. degree in science and technology for electronic and telecommunications engineering from the University of Genoa, Genoa, Italy, in 2011, 2013, and 2017, respectively. He is currently an Assistant Professor of electromagnetic fields at the Department of Electrical, Electronic, Telecommunications Engineering, and Naval Architecture, University of Genoa. His research activities are mainly focused on computational methods for the solution of forward and inverse scattering problems, and electromagnetic imaging. He has coauthored more than 100 scientific contributions published in international journals and conference proceedings. Dr. Fedeli is member of the IEEE Antennas and Propagation Society, the Italian Society of Electromagnetism, and the Inter-University Research Center on the Interactions between Electromagnetic Fields and Biosystems.

Alessandro Fanti received the Laurea degree in electronic engineering and Ph.D. degree in Electronic Engineering and computer science from the University of Cagliari, Cagliari, Italy, in 2006 and 2012, respectively. He worked as post-doctoral fellow in the Electromagnetic Group at the University of Cagliari from 2013 to 2016, where he is currently an Assistant Professor. His research activity involves the use of numerical techniques for modes computation of guiding structures, optimization techniques, analysis and design of waveguide slot arrays, analysis and design of patch antennas, radio propagation in urban environment, modeling of bio-electromagnetic phenomena, microwave exposure systems for biotechnology and bio-agriculture. He is an Associate Editor of the IEEE Journal of Electromagnetics, RF and Microwaves in Medicine and Biology (J-ERM).

Matteo Bruno Lodi (Student Member, IEEE) received the bachelor's degree in biomedical engineering from the University of Cagliari, Cagliari, in 2016, and the master's degree in biomedical engineering from Politecnico di Torino, Turin, Italy, in 2018. He is currently working toward the Ph.D. degree in electronic engineering and computer science at the University of Cagliari. His research activity deals with the modeling of bioelectromagnetic phenomena, especially hyperthermia treatment; the study, manufacturing, and synthesis of magnetic biomaterials for tissue engineering applications; and the use of microwave for biotechnology and environmental applications.

Matteo Pastorino (Fellow, IEEE) is a Full Professor of Electromagnetic Fields at the University of Genoa, Italy, where is the Director of the Department of Electrical, Electronic, Telecommunications Engineering and Naval Architecture (DITEN). From 2008 to 2011, he has been also the Director of the Department of Biophysical and Electronic Engineering (DIBE). He has authored the book Microwave Imaging (Wiley, 2010) and has coauthored the book Microwave Imaging Methods and Applications (Artech House, 2018). He has also coauthored more than 450 papers in international journals and conference proceedings. His current research interests include microwave and millimeter wave imaging, direct and inverse scattering problems, industrial and medical applications, smart antennas, and analytical and numerical methods in electromagnetism. Prof. Pastorino is currently the Chair of the National URSI Commission B (Fields and Waves), the responsible for the local section of the National Society of Electromagnetics, and the Vice Director of the Interuniversity Center for the Interaction between Electromagnetic Fields and

Biosystems. He is a member of the editorial boards and technical program committees of several international journals and conferences in the field of microwaves and antennas. He is currently an Associate Editor of the IEEE Antennas and Propagation Magazine and an Associate Editor of the IEEE Open Journal of Antennas and Propagation.

Andrea Randazzo (Senior Member, IEEE) received the laurea degree in Telecommunication Engineering from the University of Genoa, Italy, in 2001 and the Ph.D. degree in Information and Communication Technologies from the same university in 2006. Currently, he is Full Professor of Electromagnetic Fields at the Department of Electrical, Electronic, Telecommunication Engineering, and Naval Architecture of the University of Genoa. His primary research interests are in the field of microwave imaging, inverse scattering techniques, numerical methods for electromagnetic scattering and propagation, electrical tomography, and smart antennas. He has coauthored the book Microwave Imaging Methods and Applications (Artech House, 2018) and more than 250 papers published in journals and conference proceedings.